Surface Solar Irradiance in Continental Shallow Cumulus Fields: Observations and Large-Eddy Simulation

JAKE J. GRISTEY

Cooperative Institute for Research in Environmental Sciences, University of Colorado Boulder, and Chemical Sciences Division, NOAA/Earth System Research Laboratory, Boulder, Colorado

GRAHAM FEINGOLD

Chemical Sciences Division, NOAA/Earth System Research Laboratory, Boulder, Colorado

IAN B. GLENN

Cooperative Institute for Research in Environmental Sciences, University of Colorado Boulder, and Chemical Sciences Division, NOAA/Earth System Research Laboratory, Boulder, Colorado

K. SEBASTIAN SCHMIDT AND HONG CHEN

Laboratory for Atmospheric and Space Physics, University of Colorado Boulder, Boulder, Colorado

(Manuscript received 23 September 2019, in final form 4 December 2019)

ABSTRACT

This study examines shallow cumulus cloud fields and their surface shortwave radiative effects using large-eddy simulation (LES) along with observations across multiple days at the Atmospheric Radiation Measurement Southern Great Plains atmospheric observatory. Pronounced differences are found between probability density functions (PDFs) of downwelling surface solar irradiance derived from observations and LES one-dimensional (1D) online radiation calculations. The shape of the observed PDF is bimodal, which is only reproduced by offline three-dimensional (3D) radiative transfer calculations, demonstrating PDF bimodality as a 3D radiative signature of continental shallow cumuli. Local differences between 3D and 1D radiative transfer calculations of downwelling surface solar irradiance are, on average, larger than 150 W m^{-2} on one afternoon. The differences are substantially reduced when spatially averaged over the LES domain and temporally averaged over the diurnal cycle, but systematic 3D biases ranging from 2 to 8 W m^{-2} persist across different days. Covariations between the domain-averaged surface irradiance, framed as a surface cloud radiative effect, and the simulated cloud fraction are found to follow a consistent diurnal relationship, often exhibiting hysteresis. In contrast, observations show highly variable behavior. By subsampling the LES domain, it is shown that this is due to the limited sampling density of inherently 3D observations. These findings help to define observational requirements for detecting such relationships, provide valuable insight for evaluating weather and climate models against surface observations as they push to ever higher resolutions, and have important implications for future assessments of solar renewable energy potential.

1. Introduction

The Earth–atmosphere system is primarily driven by solar energy absorbed at the surface (Stephens et al. 2012; Wild et al. 2015; Trenberth and Fasullo 2012). Cloud cover is usually the most important factor modulating the amount of solar energy that reaches the surface, but understanding and modeling the processes by which broken clouds control surface solar energy variability can be nontrivial (Lane et al. 2002). Shallow cumulus clouds present a particular challenge due to their small spatial scale and rapid temporal evolution (Berg and Kassianov 2008; Lamer and Kollias 2015). Since shallow cumuli frequently populate both continental landmasses and oceanic trade wind regions,

Denotes content that is immediately available upon publication as open access.

Corresponding author: Jake J. Gristey, jake.j.gristey@noaa.gov

DOI: 10.1175/JAS-D-19-0261.1

© 2020 American Meteorological Society. For information regarding reuse of this content and general copyright information, consult the AMS Copyright Policy (www.ametsoc.org/PUBSReuseLicenses).

Downloaded from http://journals.ametsoc.org/jas/article-pdf/77/3/1065/4922254/jasd190261.pdf by NOAA Central Library user on 23 June 2020

understanding the processes controlling surface solar energy variability in these conditions is of great interest for weather and climate modeling (Burleyson et al. 2015), and for the renewable energy industry (Perez et al. 2016).

Large-eddy simulation (LES) has been widely used to study shallow cumulus cloud field properties and processes. Applications include parameterization development (Angevine et al. 2018), retrieval testing (Fielding et al. 2014), and observing system simulations (Oue et al. 2016). However, notable biases have been documented between LES output and surface observations of shallow cumuli, depending on the model setup and the datasets used to drive the simulations (Zhang et al. 2017). Surface observations themselves, although directly tied to reality, often suffer from representativeness issues as they may only sample a small portion of a much wider shallow cumulus cloud field on any given day. With these issues in mind, the LES Atmospheric Radiation Measurement (ARM) Symbiotic Simulation and Observation workflow (LASSO) project (Gustafson et al. 2019, 2020) is routinely bringing together ARM observations with LES at similar scales. Thus far, LASSO has focused on shallow convection at the Southern Great Plains (SGP) atmospheric observatory, providing an opportunity to investigate continental shallow cumulus surface cloud radiative effects in detail across multiple days.

One approach to understand the radiative effects of broken clouds is to examine the probability distribution of downwelling surface solar irradiance. Under continental shallow cumuli, this probability distribution has been observed to be bimodal (Schmidt et al. 2009). As will be discussed later, bimodality is not always present in downwelling surface solar irradiance output from LES but did emerge in three-dimensional (3D) radiative transfer calculations by Schmidt et al. (2009). Shortwave 3D radiative effects have been studied in detail for specific cloud types including deep convection (Di Giuseppe and Tompkins 2003), midlatitude cirrus (Zhong et al. 2008), and aircraft contrails (Forster et al. 2012; Gounou and Hogan 2007). The 3D radiative effect of shallow clouds has also received attention (Pincus et al. 2005; Benner and Evans 2001; Hinkelman et al. 2007), and recent evidence suggests that the shifting of cloud shadows in a 3D world can influence shallow cumulus organization (Jakub and Mayer 2017; Xiao et al. 2018; Gronemeier et al. 2017). However, the possibility of a 3D influence on the probability distribution of downwelling surface solar irradiance has not been documented and warrants further investigation.

Another complementary and increasingly popular approach to understand the radiative effects of broken clouds is to examine the relationship between scene albedo and cloud fraction. This relationship has proved a powerful framework for evaluating climate model output and has been argued to be linear (Bender et al. 2011), near exponential (Engström et al. 2015), and a combination of both depending on the cloud regime (Feingold et al. 2017). From a surface perspective, scene albedo is not readily observed, but surface radiative fluxes can be used to estimate a surface-based cloud radiative effect (Xie et al. 2014). It follows that an analogous relationship at the surface, namely, that between surface cloud radiative effect and cloud fraction, can be investigated. While long-term statistics of cloud, aerosol, and their surface radiative effects have recently been provided at SGP (Sena et al. 2016), leveraging this framework to examine observations and simulations of individual cases at the process level remains elusive.

Exploiting the synergy of LES and observations emerging from LASSO, and motivated by the aforementioned approaches to investigate shallow cumulus cloud fields and their radiative effects, the aim of the current study is twofold:

1) present probability distributions of downwelling surface solar irradiance in LES and observations and understand the role of 3D radiative effects in determining these distributions, and
2) identify and reconcile the diurnal evolution of the surface cloud radiative effect–cloud fraction relationship between LES and observations.

Both aims heed the call for a balance between detailed process understanding and high-order analyses (Feingold et al. 2016) by focusing on emergent relationships that encapsulate important information on the cloud field.

The remainder of the manuscript addresses these aims as follows. Section 2 describes the LES output and observational data used. Section 3 outlines our approach to processing and analyzing the data. Section 4 presents our key findings focusing on a case-study day and extends these findings to multiple days. Finally, section 5 summarizes the study and outlines directions for future work.

2. Data

Four study days spanning the summers of 2015–17 are selected from the LASSO data stream for consideration (Table 1). These four study days are selected to represent ''classic'' shallow cumulus days at SGP that are well reproduced by our simulations. That is, they

Downloaded from http://journals.ametsoc.org/jas/article-pdf/77/3/1065/4922254/jasd190261.pdf by NOAA Central Library user on 23 June 2020

TABLE 1. "Classic" shallow cumulus days selected from the LASSO data stream that are considered in this study. The case-study day is in italics.

2015	2016	2017
27 Jun	25 Jun	14 Jun 17 Jul

are primarily locally driven by the diurnal cycle of incoming solar radiation, start and end the day with cloud-free skies, reach only modest cloud fraction by midafternoon, and have no accompanying ice cloud. Several data sources—including surface sky imagery, geostationary satellite imagery, and simulated cloud field properties—were used to identify and exclude days that do not meet these criteria. Afternoon total-sky images for the study days (ARM 2019b) are shown in Fig. 1.

a. LES output

For each of the four study days listed in Table 1, we ran LES using version 6.10.10 of the System for Atmospheric Modeling (SAM) (Khairoutdinov and Randall 2003). SAM simulations were initialized with vertical profiles obtained from 1200 UTC radiosonde soundings at the SGP Central Facility, and forced by prescribed surface fluxes and large-scale advective tendencies from the ARM constrained variational analysis (VARANAL) product (Xie et al. 2004). In contrast to standard LASSO LES, the microphysical activation in our simulations includes a representation of spatial and temporal aerosol variability informed by the Condensation Nuclei Counter and Cloud Condensation Nuclei Counter at SGP. Observations from those instruments were used to constrain the aerosol size distribution and diurnal variation of total aerosol number, respectively; further details are given in Glenn et al. (2019, manuscript submitted to *J. Atmos. Sci.*).

The LES was run from 0700 to 2200 local time (LT; central daylight time or UTC − 5 h) on each study day with a horizontal grid spacing of 100 m and a vertical grid spacing equal to 30 m below 5 km, incrementally stretched to 300 m by 10 km, continuing to 15-km altitude. The domain size is 24 km × 24 km × 15 km, and the dynamical time step is half a second. Interactive radiation calculations within SAM are performed once every simulated minute by the Rapid Radiative Transfer Model with improved efficiency for general circulation model applications (RRTMG; Mlawer et al. 1997; Clough et al. 2005). The RRTMG calculations employ a plane-parallel independent column approximation (PP-ICA), henceforth referred to as one-dimensional (1D) radiative transfer. While we also investigate 3D radiative effects, note that 3D calculations are performed offline and not coupled to the LES (see section 3), which could influence organization in the cloud field (Jakub and Mayer 2017; Xiao et al. 2018). For this study, we use two-dimensional output of all-sky and clear-sky downwelling surface solar irradiance as calculated by RRTMG every minute, along with cloud fraction defined based on an optical depth of unity. This constant optical depth threshold provides a fundamental measure of cloud amount, but we found that our results are consistent if we alternatively divide the optical depth threshold by the cosine of the solar zenith angle, which is more relevant to the cloud shadow darkness (Glenn et al. 2019, manuscript submitted to *J. Atmos. Sci.*). We also use 3D output of liquid water content and cloud droplet number concentration every 10 min.

For our case-study day, 27 June 2015, we performed two additional simulations for the purpose of sensitivity tests. First, we performed an identical simulation but with quadruple horizontal resolution (50 m in both horizontal dimensions) to determine sensitivity to resolution. Second, we performed an identical simulation but with quadruple domain area (48 km × 48 km) to determine sensitivity to domain extent.

b. ARM observations

To compare with the LES output, observations at the ARM SGP atmospheric observatory are obtained for each of the four study days listed in Table 1. Specifically, we extracted the all-sky and clear-sky downwelling surface solar irradiance, and cloud fraction, from the Radiative Flux Analysis (RFA) value-added product (ARM 2019a). All data have a temporal resolution of 1 min. While the downwelling surface solar irradiance is directly observed, the clear-sky downwelling surface solar irradiance and cloud fraction are retrieved quantities (Long and Ackerman 2000; Long et al. 2006). The estimated uncertainty (95% confidence interval) in the downwelling surface solar irradiance is 6% or 10 W m^{-2}, whichever is the greater number (Stoffel 2005), while the retrieved clear-sky root-mean-square error (RMSE) is approximately double the measurement uncertainty, and the retrieved cloud fraction RMSE is better than 10% when compared against sky imager retrievals and human observations. We found the RFA cloud fraction to be in good agreement with the total-sky imager cloud fraction at the SGP Central Facility (not shown), but we chose to use the RFA cloud fraction because it

Downloaded from http://journals.ametsoc.org/jas/article-pdf/77/3/1065/4922254/jasd190261.pdf by NOAA Central Library user on 23 June 2020

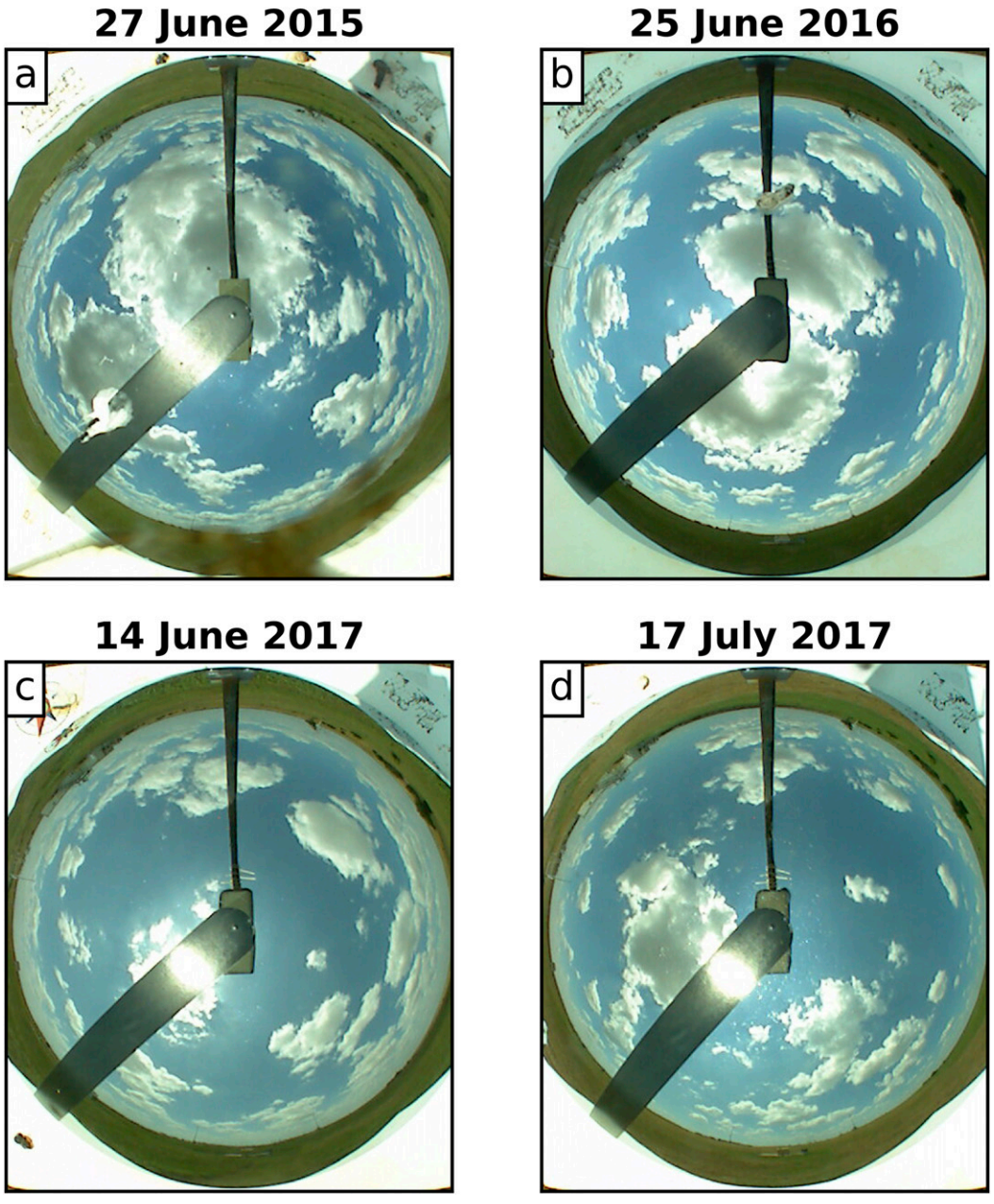

FIG. 1. Total-sky imager snapshots from the ARM SGP atmospheric observatory central facility at 1430 local time (UTC − 5 h) on the days considered in this study.

is available at more locations and we expect it is more consistent with the observed downwelling surface solar irradiance.

The RFA observations are extracted at the ARM SGP Central Facility and nine other extended facilities within ~150 km × 150 km surrounding the central facility (Fig. 2). While the region that the observations occupy is larger than the LES domain size, recall that our LES is forced by VARANAL datasets that represent conditions over a 300 km × 300 km region, which encompasses all of the observations considered here.

3. Method

Two distinct approaches are pursued to investigate shallow cumulus cloud fields and their surface radiative effects. First, we focus on probability distributions of the downwelling surface solar irradiance. As will be shown in section 4a(1), stark differences exist between the

Downloaded from http://journals.ametsoc.org/jas/article-pdf/77/3/1065/4922254/jasd190261.pdf by NOAA Central Library user on 23 June 2020

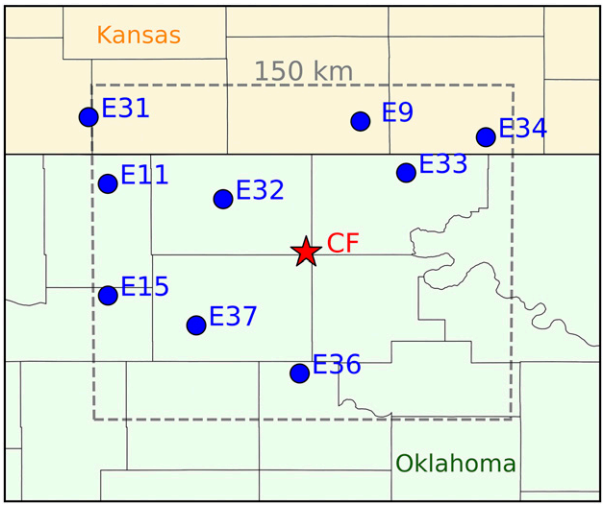

FIG. 2. A map of the central facility (CF; red star) and extended facilities (blue circles) at the ARM SGP atmospheric observatory, from which observations are obtained for this study. The map is centered on the CF, which is located at 36.605°N, 97.485°W.

probability density functions (PDFs) of observed and simulated downwelling surface solar irradiance using LES online 1D radiation output. Based on the agreement between observations and 3D radiative transfer calculations for shallow continental cumulus clouds previously documented in Houston, Texas (Schmidt et al. 2009), we hypothesize that 3D radiative effects play a key role in these PDF differences.

Since horizontal photon transport is unaccounted for in our LES output, we assess the importance of 3D radiative effects by performing an additional set of offline 3D radiative transfer calculations of the downwelling surface solar irradiance (direct, diffuse and total components). To do this, the 3D LES cloud fields (liquid water content and number concentration) are used as input to the Education and Research 3D Radiative Transfer Toolbox (EaR3T), which is a newly developed Python interface to the Monte Carlo Atmospheric Radiative Transfer Simulator (MCARaTS) (Iwabuchi 2006). EaR3T was originally developed as a line-by-line 3D code to simulate radiances for the *Orbiting Carbon Observatory* (*OCO-2*; K. S. Schmidt et al. 2019, unpublished manuscript). For this work, it was adapted for moderate-resolution (4–8 nm) calculations based on a correlated-k approach by Coddington et al. (2008). The calculations are performed three times for each 3D LES snapshot: once with full 3D radiative transfer, once with 1D radiative transfer, and once without cloud. Calculations at 5-nm spectral resolution from 350 to 2200 nm (encompassing >95% of the incoming energy) are integrated via the trapezoidal rule to obtain broadband quantities. Three simulations for each wavelength, each containing one million photons scaled by the magnitude of the top-of-atmosphere incoming solar irradiance ($\mathrm{W\,m^{-2}}$) at the corresponding wavelength are averaged to obtain the downwelling surface solar irradiances. Horizontally homogeneous trace gas profiles from the standard midlatitude summer atmosphere (McClatchey et al. 1972) are used in all 3D calculations.

To quantify the influence of 3D radiative effects on PDFs of downwelling surface solar irradiance, we examine differences between the offline 3D and 1D radiative transfer calculations outlined above. Spatial and temporal differences in diffuse and direct components, as well as the total downwelling surface solar irradiance, are examined. The variation of these separate components in relation to the cloud field provides additional information on where and how radiation is scattered throughout the domain, and therefore further insight into the processes at play.

To address scale differences between observations (near-instantaneous locally sensitive measurements) and LES (spatiotemporally averaged quantities), we calculate simulated differences as a function of spatial and temporal averaging scale. The difference as a function of spatial averaging scale σ_s is calculated as

$$\sigma_S = \frac{\sum_{i=0}^{X}\sum_{j=0}^{Y}\left|\frac{\sum_{k=-S/2}^{S/2}\sum_{l=-S/2}^{S/2}F^{\downarrow}_{3\mathrm{D}}(x_{i+k},y_{j+l})}{S^2}-\frac{\sum_{k=-S/2}^{S/2}\sum_{l=-S/2}^{S/2}F^{\downarrow}_{1\mathrm{D}}(x_{i+k},y_{j+l})}{S^2}\right|}{XY}, \quad (1)$$

where $F^{\downarrow}_{3\mathrm{D}}$ and $F^{\downarrow}_{1\mathrm{D}}$ are the downwelling surface solar irradiances from 3D and 1D calculations, respectively; x and y are locations in a domain with X and Y horizontal grid points; and S is the number of horizontal grid points over which the spatial averaging occurs.

Downloaded from http://journals.ametsoc.org/jas/article-pdf/77/3/1065/4922254/jas190261.pdf by NOAA Central Library user on 23 June 2020

If time evolving radiation rather than snapshots are considered, then the difference as a function of temporal averaging scale σ_T is calculated as

$$\sigma_T = \frac{\sum_{i=0}^{X}\sum_{j=0}^{Y}\left|\frac{\sum_{t=-T/2}^{T/2} F^{\downarrow}_{3D}(x_i, y_j, t)}{T} - \frac{\sum_{t=-T/2}^{T/2} F^{\downarrow}_{1D}(x_i, y_j, t)}{T}\right|}{XY}, \tag{2}$$

where t is time interval, and T is the number of 10-min time intervals over which the temporal averaging occurs.

Our second approach to analyzing shallow cumulus cloud radiative effects is to examine the relationship between relative cloud radiative effect (rCRE) and cloud fraction f_C, providing a perspective from radiatively relevant macroscale properties that are readily obtained from both simulations and observations. The rCRE (sometimes referred to as an effective cloud albedo) provides an instantaneous measure of the extent to which clouds block solar radiation from reaching the surface (Sena et al. 2016; Betts and Viterbo 2005; Liu et al. 2011). Written as a percentage, rCRE is defined as

$$\text{rCRE} = \left(1 - \frac{F^{\downarrow}}{F^{\downarrow}_{\text{CLR}}}\right) \times 100, \tag{3}$$

where $F^{\downarrow}$ is the downwelling surface solar irradiance (W m^{-2}); and $F^{\downarrow}_{\text{CLR}}$ is the corresponding clear-sky downwelling surface solar irradiance (W m^{-2}). Since the rCRE defined in Eq. (3) contains a normalization by $F^{\downarrow}_{\text{CLR}}$, it is less sensitive to variations in the amount of incoming radiation at the top of the atmosphere, enabling meaningful comparisons throughout any given day. A rCRE value of 100% would imply that clouds block all solar radiation from reaching the surface, while a value of 0% would imply that clouds have no effect on the downwelling surface solar irradiance.

In LES, unless otherwise stated, rCRE and f_C are considered as domain-scale quantities. It follows that rCRE–f_C relationships represent a holistic view of diurnally evolving shallow cumulus cloud fields and their radiative effects. For improved comparison with LES domain mean quantities, we experiment with spatiotemporal averaging of the observations. First, a 1-h running mean is applied, chosen to be much longer than typical sky-view decorrelation time scales on the order of 15 min (Kassianov et al. 2005). Then, we perform a spatial mean of the observations across all of the extended facilities within ~150 km of the central facility (Fig. 2). The appropriateness and consequences of this spatiotemporal averaging are discussed in section 4a(2).

We also seek to determine the influence of 3D radiative effects on the diurnal cycle of the rCRE–f_C relationship. Using our offline 3D radiative transfer output, rCRE–f_C relationships are recalculated and compared to their 1D counterparts. By subsampling the model domain toward the sampling density of current observational networks, we isolate various factors that influence the ability of observations to detect such relationships, hence determining observational requirements.

4. Results

a. A case study: 27 June 2015

To illustrate the key characteristics of shallow cumuli and their surface radiative effects at SGP, an analysis of one particular day, 27 June 2015, is provided first. The simulated cloud field on this day begins with sparse clouds that populate the shallow early-afternoon boundary layer (Fig. 3a), followed by increased cloud coverage later in the afternoon as convection is invigorated by surface solar heating (Figs. 3b,c), and ends with rapid cloud dissipation in the evening as the surface solar heating diminishes and the boundary layer collapses (Fig. 3d). Individual clouds typically do not exceed 2 km in horizontal extent throughout the day. As the diurnal boundary layer grows, cloud-base and cloud-top heights both increase, but cloud-top height increases at a faster rate leading to deeper clouds later in the day. This relative change in cloud base and cloud top may not generally be the case (Berg and Kassianov 2008), but it is true for all days considered in this study.

This evolving cloud field (Fig. 3) causes surface radiative effects that have intricate spatial and temporal variability. In the following subsections, we investigate downwelling surface solar irradiance distributions [section 4a(1)] and rCRE–f_C relationships [section 4a(2)] to shed some light on how this variability manifests itself in both observations and our simulations.

1) PDFs of downwelling surface solar irradiance

Afternoon RFA observations during the case-study day reveal a bimodal PDF of downwelling surface solar irradiance (Fig. 4a), consistent with previous observational findings in shallow cumulus (Schmidt et al. 2009). The explanation of bimodality is relatively straightforward; the peak at smaller irradiance values is associated

Downloaded from http://journals.ametsoc.org/jas/article-pdf/77/3/1065/4922254/jasd190261.pdf by NOAA Central Library user on 23 June 2020

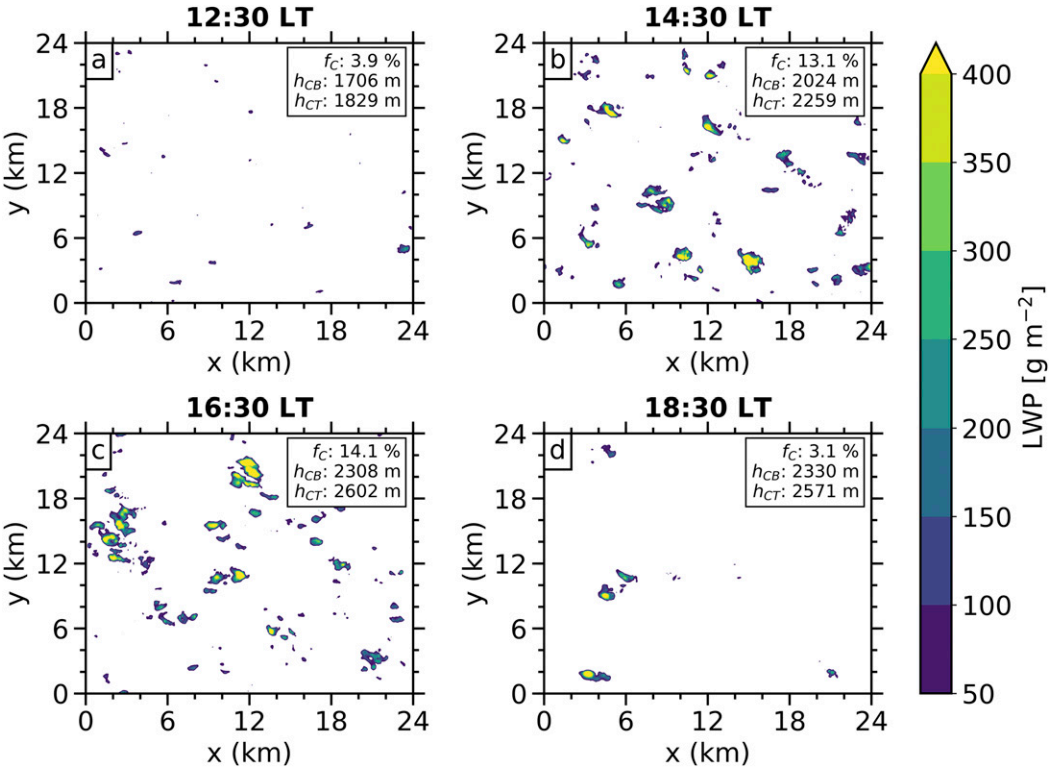

FIG. 3. LES of cloud liquid water path (LWP) at (a) 1230, (b) 1430, (c) 1630, and (d) 1830 LT (UTC − 5 h) on 27 Jun 2015 at the ARM SGP atmospheric observatory. Also given in each plot are domain mean of cloud fraction f_C, cloud-base height h_{CB}, and cloud-top height h_{CT}, all defined based on a cloud optical depth of 1.

with extinction of the direct beam beneath clouds, while the peak at larger irradiance values represents the gaps between the clouds. The detailed structure of the PDF, however, is associated with the detailed properties of the cloud field. For example, one would expect a larger proportion of the distribution to reside in the smaller irradiance peak at larger cloud fraction, or the distance between the peaks to be greater at larger cloud optical depth. Investigation of such relationships is well suited to LES where, unlike observations, the precise cloud field properties controlling surface radiation variability are known.

Ingesting the LES output for the same time window on this afternoon into our offline radiative transfer simulator yields profoundly different PDFs depending on whether 3D radiative effects are included. When 3D radiative effects are excluded (i.e., using the PP-ICA approximation similar to the RRTMG calculation performed at run time), the resulting PDF (Fig. 4b) bears little resemblance to the observed PDF (Fig. 4a). There is a sharp cutoff at large irradiance values that is not present in the observations. Likewise, the first mode of the observed PDF does not appear.

Spatial maps of the downwelling surface solar irradiance (Figs. 5a–c) reveal several features that help to understand the PDF that emerges when 3D radiative effects are excluded. Sharp cloud boundaries identified in both the direct (Fig. 5b) and diffuse (Fig. 5c) components, by definition of 1D radiative transfer, cause diffuse radiation scattered downward by any given cloud to partially fill in the reduction of the direct beam caused by the exact same part of that cloud. This reduces the overall darkness of the cloud shadows (Fig. 5a), and also means that the variation in cloud shadow darkness closely follows the transition to typically larger liquid water path at cloud centers (see Fig. 3b). Away from cloud shadows, no scattered radiation by clouds reaches the surface. As a result, a very similar irradiance magnitude is always encountered in clear-sky regions, hence the spike in the PDF at large irradiance values.

When 3D radiative effects are included, a very different PDF emerges (Fig. 4c). In contrast to the 1D calculations (Fig. 4b), but similar to the observed PDF (Fig. 4a), bimodality is present, and the peak at larger irradiance values exhibits a tail toward maximum values. The corresponding spatial maps (Figs. 5d–f) again provide insight into the structure of this PDF. The direct component (Fig. 5e) is similar to that from the 1D calculation (Fig. 5b), other than a slight horizontal shift

Downloaded from http://journals.ametsoc.org/jas/article-pdf/77/3/1065/4922254/jasd190261.pdf by NOAA Central Library user on 23 June 2020

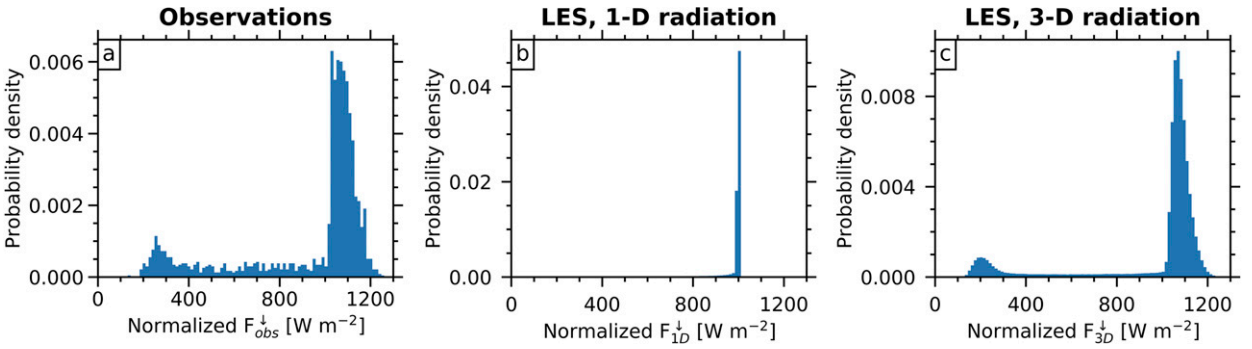

FIG. 4. Probability density functions (PDFs) of downwelling surface solar irradiance from 1300 to 1600 LT (UTC − 5 h) 27 Jun 2015 at the ARM SGP atmospheric observatory: (a) based on 1-min RFA observations $F^{\downarrow}_{\text{obs}}$ from all 10 SGP locations in Fig. 2; (b) calculated with 1D radiative transfer $F^{\downarrow}_{\text{1D}}$ using 3D LES output; and (c) calculated with 3D radiative transfer $F^{\downarrow}_{\text{3D}}$ using 3D LES output. Calculations at different times are normalized by the cosine of the solar zenith angle. Note the changes in vertical scale.

in the location of cloud shadows due to the projection of solar angle. Differences in the variability of the total field (Figs. 5a,d) therefore primarily emerge from differences in the diffuse component (Figs. 5c,f). Horizontal photon transport leads to scattered radiation by clouds reaching the surface in locations other than in the cloud shadows, causing a smoother diffuse irradiance field. The implication of this radiative smoothing is a net darkening of cloud shadows in large optical depth regions, and a net brightening in small optical depth regions (cf. Figs. 5a,d). The net darkening leads to a prevalence of small atmospheric transmittance values causing the smaller irradiance peak in the PDF (Fig. 4c), even if the distribution of optical thickness from the LES cloud field does not show any pronounced maximum (not shown). The net brightening in small optical depth regions leads to a shift in the larger irradiance peak toward larger irradiance values (cf. Figs. 4b,c). These larger irradiance values can exceed clear-sky values at the surface (e.g., Berg et al. 2011), and sometimes even exceed the top-of-atmosphere incoming irradiance. Cloud scattering toward the surfaces of surrounding clear-sky regions is increasingly enhanced toward cloud edge, leading to the tail in the larger peak of the PDF toward maximum values. Cloud brightening and darkening due to horizontal photon

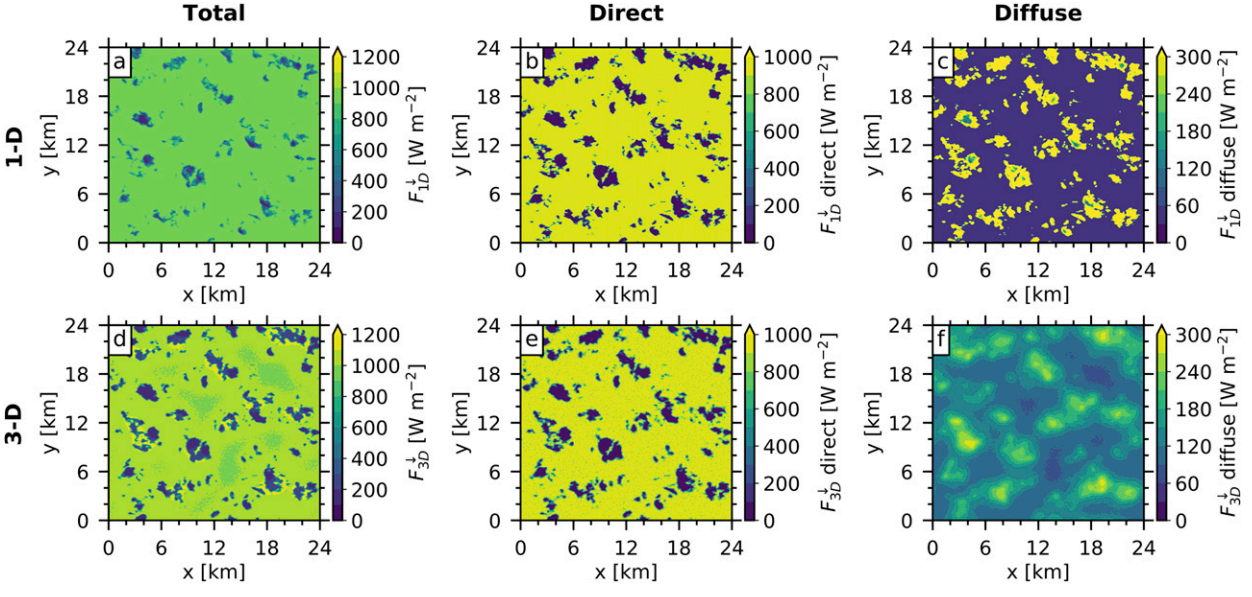

FIG. 5. Maps of simulated downwelling surface solar irradiance at 1430 LT (UTC − 5 h) 27 Jun 2015 at the ARM SGP atmospheric observatory, calculated with (a)–(c) 1D ($F^{\downarrow}_{\text{1D}}$) and (d)–(f) 3D $F^{\downarrow}_{\text{3D}}$ radiative transfer. Data are presented for (a),(d) total irradiance, along with the separate (b),(e) direct and (c),(f) diffuse components. Based on offline Monte Carlo radiative transfer that ingests 3D large-eddy simulation output.

Downloaded from http://journals.ametsoc.org/jas/article-pdf/77/3/1065/4922254/jasd190261.pdf by NOAA Central Library user on 23 June 2020

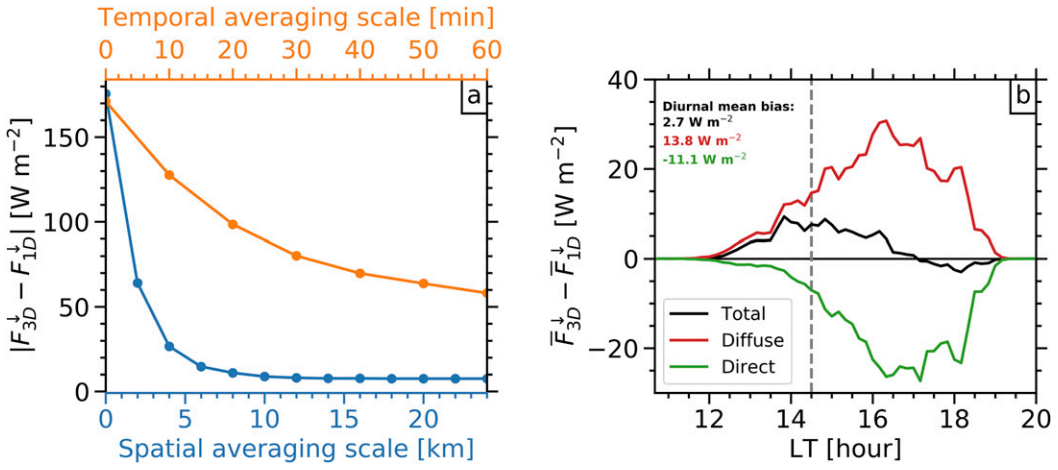

FIG. 6. Differences between downwelling surface solar irradiance calculated with 1D ($F^{\downarrow}_{1D}$) and 3D $F^{\downarrow}_{3D}$ radiative transfer on 27 Jun 2015 at the ARM SGP atmospheric observatory. (a) Absolute difference at 1430 LT (UTC − 5 h) as a function of spatial and temporal averaging scale. Note that the axis scales are aligned such that the temporal and spatial averaging scale magnitudes correspond approximately with the horizontal flow at cloud altitude. (b) Diurnal cycle of domain-mean 1D ($\overline{F}^{\downarrow}_{1D}$) and 3D ($\overline{F}^{\downarrow}_{3D}$) difference, presented as total, direct, and diffuse components. Also given in the plot are diurnal-mean biases, calculated within the time window that 3D radiative effect magnitude is above Monte Carlo noise. The gray dashed line in (b) indicates the valid time of (a).

transport can also influence top-of-atmosphere reflectance-based remote sensing, which will be explored in a future paper.

Clearly, the difference between 3D and 1D calculations of downwelling surface solar irradiance can be substantial at a single location and time. This raises the question of the scales at which these spatial and temporal differences persist, and whether systematic biases exist. Starting with the 3D and 1D downwelling surface solar irradiance fields at 1430 LT (Figs. 5a,d), and averaging them over increasingly larger spatial [Eq. (1)] and temporal [Eq. (2)] scales, we find that the absolute difference between them quickly decreases (Fig. 6a). At a single location (i.e., averaging scales of zero), the expected difference is more than 150 W m^{-2}. Note that this is substantially larger than current observational uncertainties (see section 2b). When performing temporal averaging, the decrease is relatively slow, suggesting that the cloud field is evolving faster than the rate at which the differences dissipate. However, the irradiance difference decreases by an order of magnitude when spatially averaged over approximately 5–10 km. This finding is remarkably similar to the rate of decrease previously found in net horizontal photon transport (Song et al. 2016), surface irradiance calculations for fixed cloud scenes (O'Hirok and Gautier 2005), and the spatial scale that 3D and 1D differences converge in satellite observations (Ham et al. 2014), despite the different cloud regimes considered in those studies. The irradiance difference asymptotes soon after 10-km spatial averaging scale but remains around 8 W m^{-2} even when averaged over the domain-mean scale of 24 km. The fact that the domain-mean difference at 1430 LT is nonzero suggests that 3D radiative effects can systematically perturb the surface energy budget.

Since 3D radiative effects can manifest themselves via different mechanisms whose relative importance can be a strong function of solar angle (e.g., Várnai and Davies 1999; Várnai 2000; Hogan and Shonk 2013), we conclude this section by considering the domain-mean 3D and 1D difference in downwelling surface solar irradiance over the entire diurnal cycle. Throughout most of the afternoon, when the sun is high in the sky, there is a positive 3D radiative effect (Fig. 6b, black line). This is driven by the diffuse irradiance difference (Fig. 6b, red line), consistent with the scattering by clouds into surrounding clear-sky regions shown earlier (Fig. 5), or the "side escape" mechanism at small solar zenith angles. Another recently proposed mechanism coined "entrapment" (Hogan et al. 2019) could also play a role; entrapment accounts for the trapping of radiation between multilayered interfaces resulting from horizontal photon transport. Due to our single-layer cloud cases, entrapment is only expected to be relevant for scattering between cloud-surface interfaces. To isolate the influence of entrapment, we repeated our 3D radiative transfer calculations with a smaller spectrally constant surface albedo of 0.06 (representative of an ocean surface) and found that the diurnal-mean diffuse component changed by around 15% (not shown). This suggests that while entrapment

Downloaded from http://journals.ametsoc.org/jas/article-pdf/77/3/1065/4922254/jasd190261.pdf by NOAA Central Library user on 23 June 2020

is not the dominant mechanism controlling the diffuse radiation, it can play a significant role in the total 3D radiative effect. Toward the end of the day there is a smaller negative 3D effect (Fig. 6b, black line). In contrast, this is driven by the direct irradiance difference (Fig. 6b, green line), as expected from the "side illumination" mechanism when the sun is low in the sky (Hogan and Shonk 2013).

Averaged over the entire diurnal cycle, we find the positive 3D effect dominates, and a 2.7 W m^{-2} bias exists in the total downwelling surface solar irradiance. This results from substantially larger magnitude direct and diffuse biases that act in opposite directions. In contrast to many earlier studies that have focused on the mechanisms for 3D radiative effects, these results simultaneously consider the diurnal evolution of solar angle *and* the underlying cloud field (which is explicitly resolved by the LES), providing a realistic assessment of the impact of neglecting 3D radiative transfer in shallow cumulus cloud fields.

2) rCRE–f_C

Having first established confidence in simulated surface irradiance fields once 3D effects are accounted for, we now proceed to investigate relationships between this surface irradiance variability and cloud field properties. Many features of the *simulated* cloud field and its surface radiative effects are captured concisely by the diurnally evolving rCRE–f_C relationship (Fig. 7). Perhaps the most pertinent feature present in this relationship is the diurnal hysteresis; as f_C is increasing during the morning and early afternoon, it is associated with smaller rCRE than when f_C is decreasing during the late-afternoon and evening. The extent of the hysteresis is a direct result of diurnal changes in the cloud field properties (e.g., deeper clouds at the same cloud fraction in the evening), and therefore provides useful insight into the evolution of the cloud field and its associated radiative effect.

Also of note in the simulated rCRE–f_C relationship (Fig. 7) are the minor departures, or "wiggles," in the otherwise smooth transitions from one time to the next (e.g., around 1800 LT). Of the two sensitivity simulations performed, the quadruple-horizontal-resolution simulation showed a very similar rCRE–f_C relationship, but the quadruple-domain-size simulation resulted in a suppression of the wiggles (Fig. 7, gray line). This suggests the wiggles are likely stochastic in nature and related to the limited domain size.

The corresponding *observed* rCRE–f_C relationship derived from "raw" RFA observations at the SGP Central Facility (Fig. 8a) is extremely noisy and shows little to no resemblance with the simulated

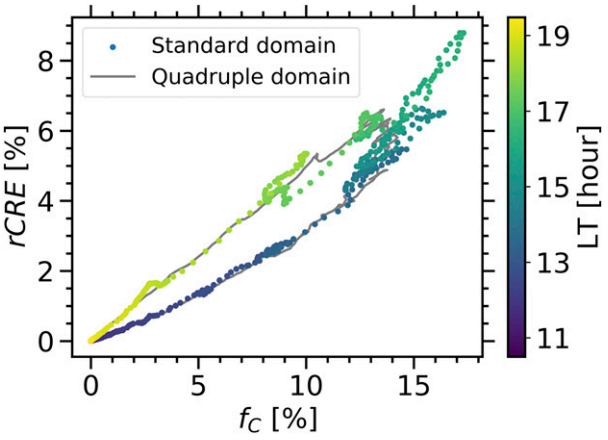

FIG. 7. LES of the diurnal relationship between relative cloud radiative effect (rCRE) and cloud fraction (f_C) on 27 Jun 2015 at the ARM SGP atmospheric observatory. The quadruple-domain-size simulation (gray line) has similar diurnal timing to the standard domain (colored dots).

relationship. This noisy relationship results mostly from the fact that the observations are 1-min averages, causing sudden jumps in rCRE when a cloud passes between the instrument and the sun. Also note that the rCRE is often negative, resulting from the diffuse enhancement caused by clouds scattering radiation into the more frequent surrounding clear-sky regions and enhancing the downwelling surface solar irradiance relative to clear-sky (see Fig. 5). These issues are alleviated when a 1-h running mean is applied to the data (Fig. 8b) resulting in smoother transitions from one time to the next. However, the diurnal evolution of the rCRE–f_C relationship remains rather random. When, additionally, the data are spatially averaged over the SGP extended facilities (Fig. 8c), a more consistent diurnal increase and decrease in both rCRE and f_C emerges. However, even with this spatiotemporal averaging of observations, the hysteresis identified in LES (Fig. 7) does not emerge.

To further examine the discrepancies in the rCRE–f_C relationship between observations and simulations, we next consider 3D radiative effects and sampling density. First, we note that the inclusion of 3D radiative effects in our simulated cloud fields is not sufficient to explain the lack of hysteresis in the observed rCRE–f_C relationship when sampling density is high, and even appears to enhance the hysteresis (cf. Figs. 9a,d). Minor deviations in the rCRE–f_C relationships depend on the specific locations included, but the overall shape is consistent when results are repeated with a different set of random locations. Subsetting the model output at just 10 random grid points to more closely match the

Downloaded from http://journals.ametsoc.org/jas/article-pdf/77/3/1065/4922254/jasd190261.pdf by NOAA Central Library user on 23 June 2020

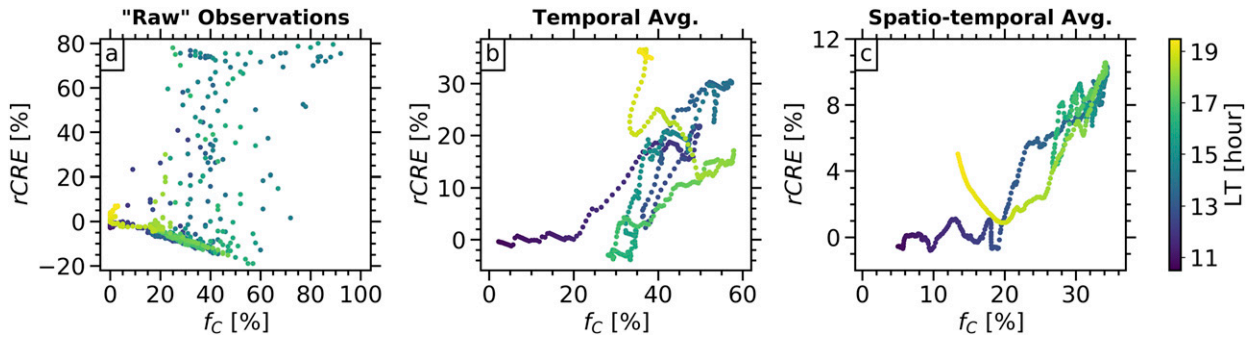

FIG. 8. Observations of the diurnal relationship between relative cloud radiative effect (rCRE) and cloud fraction (f_C) on 27 Jun 2015 at the ARM SGP atmospheric observatory for various spatiotemporal averaging scales. Data are presented (a) at the ARM SGP central facility at their native 1-min temporal resolution, (b) smoothed with a 1-h running mean, and (c) smoothed with a 1-h running mean and averaged across the 10 SGP locations shown in Fig. 2.

observational sampling pattern also does not lead to a complete breakdown of the simulated rCRE–f_C relationship (cf. Figs. 9a,c). However, the combination of 3D effects and limited sampling leads to a rCRE–f_C relationship substantially more variable than either of the individual influences (Fig. 9f), which is more consistent with the behavior found in observations.

In summary, it is found that great care must be taken regarding spatiotemporal averaging for meaningful comparisons of the diurnal evolution of shallow cumulus and their surface radiative effects between observations and LES output. Even when data are appropriately averaged, 3D radiative effects need to be accounted for. While the combination of LES and 3D radiative transfer indicates that PDFs of surface radiation can be simulated well (Fig. 4), fundamental limitations remain for capturing rCRE–f_C relationships due to the sampling density of even our most heavily instrumented surface observation networks. The results suggest an observational requirement for an order of magnitude increase in sampling density to capture this relationship. This highlights the value of process

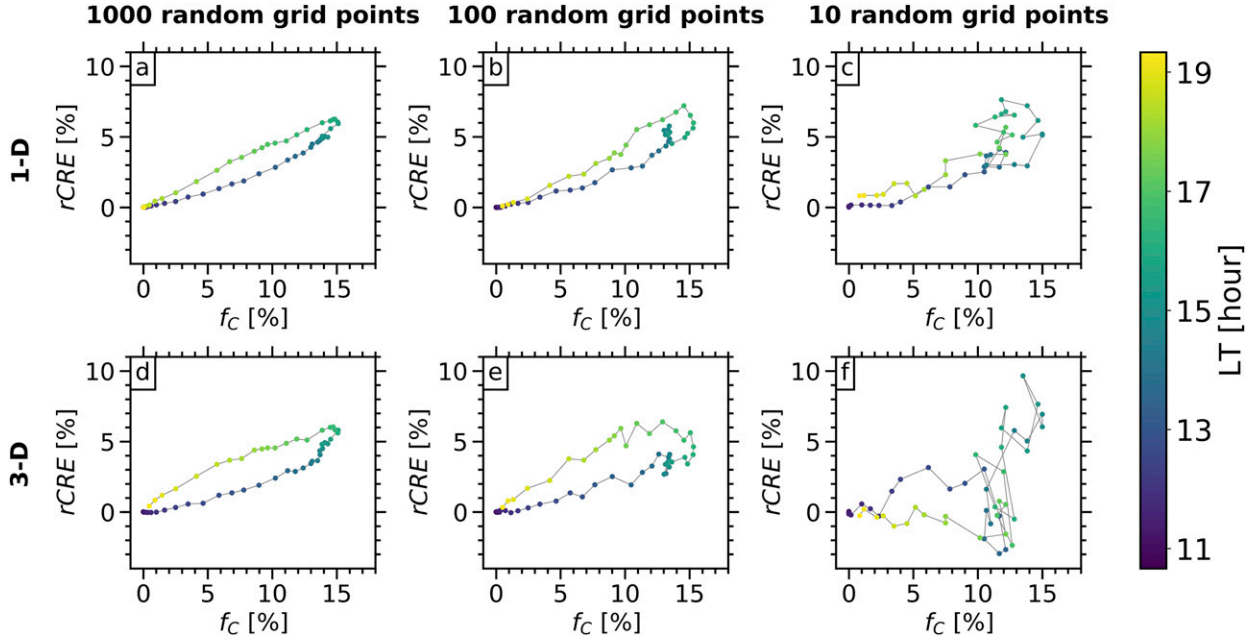

FIG. 9. Simulated diurnal relationships between relative cloud radiative effect (rCRE) and cloud fraction (f_C) on 27 Jun 2015 at the ARM SGP atmospheric observatory, calculated with (a)–(c) 1D and (d)–(f) 3D radiative transfer. Data are presented as a function of random sampling density at (a),(d) 1000, (b),(e) 100, and (c),(f) 10 grid points. The rCRE calculations are performed offline using Monte Carlo radiative transfer that ingests the 3D LES output, while f_C is retained from the LES. Each data point is a 1-h running mean, consistent with the processed observations in Fig. 8c.

Downloaded from http://journals.ametsoc.org/jas/article-pdf/77/3/1065/4922254/jasd190261.pdf by NOAA Central Library user on 23 June 2020

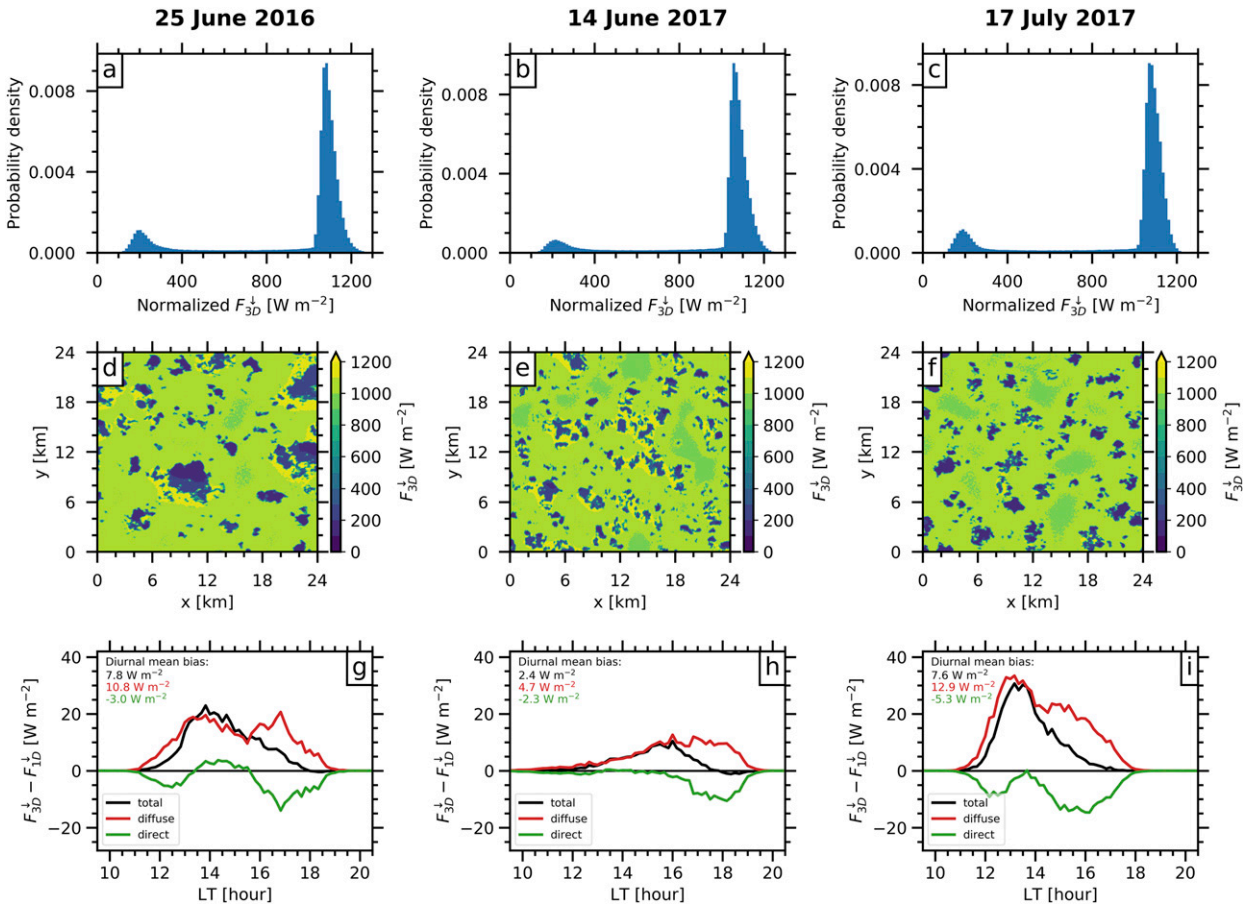

FIG. 10. (a)–(c) PDFs of simulated downwelling surface solar irradiance calculated with $F_{3D}^{\downarrow}$, (d)–(f) spatial maps of $F_{3D}^{\downarrow}$, and (g)–(i) diurnal differences between $\overline{F}_{3D}^{\downarrow}$ and $\overline{F}_{1D}^{\downarrow}$. These plots are similar to Figs. 4c, 5d, and 6b, respectively, but correspond to the three non-case-study days listed in Table 1. PDFs contain data from 1300 to 1600 LT (UTC − 5 h) that are normalized by the cosine of the solar zenith angle at each time. Spatial maps are valid at 1430 LT.

investigations via high-resolution modeling that are not always accessible from observations.

b. *Extension to multiple days across 2015–17*

To provide a broader perspective to the case study presented in the previous section, we now consider statistics over multiple shallow cumulus days (Table 1). PDFs of downwelling surface solar irradiance from 3D calculations on the non-case-study days all exhibit bimodal structure (Figs. 10a–c), consistent with the case-study day. The shape and magnitude of the PDFs are remarkably similar across different days. Since the simulated cloud fraction does not exceed 20% on any of the days, the smaller irradiance peak in the PDFs always represents less data than the larger irradiance peak. The small cloud fraction can be seen in the spatial maps of downwelling surface solar irradiance (Figs. 10d–f) where the diffuse enhancement around cloud edge is also evident. Clear differences in individual cloud sizes between the days do not appear to strongly influence the shape of the PDFs, but subtle differences (e.g., the slightly flatter smaller irradiance peak on 14 June 2017) could hold important information regarding cloud field properties.

The diurnal cycle of domain-mean differences between 3D and 1D calculations on the non-case-study days (Figs. 10g–i) have many similar characteristics to the case-study day but also a few important differences. The diurnal-mean difference is always positive and driven primarily by large positive diffuse differences that dominate in the early afternoon. The direct difference is usually negative, but one feature not seen on the case-study day is the increase, and even positive, direct difference for a short period during midafternoon. Preliminary calculations suggest that the mechanism for a direct positive 3D effect at the surface is nontrivial and will be investigated further in future work. The magnitude of the domain-mean diurnal-mean difference

Downloaded from http://journals.ametsoc.org/jas/article-pdf/77/3/1065/4922254/jas190261.pdf by NOAA Central Library user on 23 June 2020

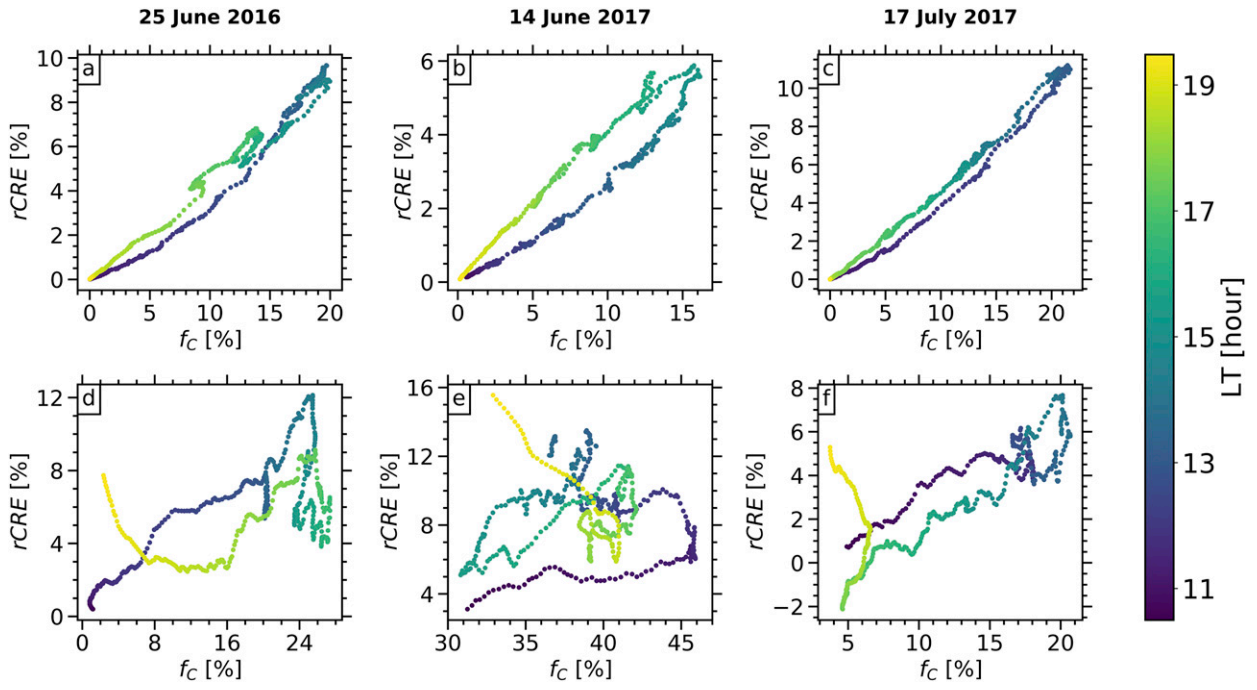

FIG. 11. (a)–(c) LES of the diurnal relationship between relative cloud radiative effect (rCRE) and cloud fraction (f_C) at the ARM SGP atmospheric observatory. (d)–(f) Observations of the diurnal relationship between rCRE and f_C at the ARM SGP atmospheric observatory, smoothed with a 1-h running mean and averaged across the 10 SGP locations shown in Fig. 2. These plots are similar to Figs. 7 and 8c, respectively, but correspond to the three non-case-study days listed in Table 1.

varies approximately by a factor of 3, reaching almost 8 W m^{-2} on 25 June 2016 and 17 July 2017.

The rCRE–f_C relationships derived from LES on these additional non-case-study days (Figs. 11a–c) all exhibit an ascending morning branch and descending evening branch with varying extent of separation, or diurnal hysteresis. For example, 14 June 2017 exhibits strong hysteresis, but 17 July 2017 exhibits very little hysteresis, representing important variations in the evolution of the cloud fields. Again consistent with the case-study day, spatiotemporally averaged observations (Figs. 11d–f) do not reproduce the rCRE–f_C diurnal hysteresis seen in LES on any of the non-case-study days. Note that the observed relationship on 14 June 2017 (Fig. 11e) comprises worse statistics because we excluded extended facility E37 due to a cloud fraction retrieval error (appearing in the data stream as a fixed 100% cloud fraction throughout most of the day).

While the observations otherwise capture the general increase and decrease in rCRE and f_C on all of these days, there are some systematic differences that stand out when compared to LES. First, the magnitude of f_C is consistently larger in observations. This is at least partly due to the difference between hemispheric sky cover obtained from RFA and nadir cloud fraction obtained from LES (Kassianov et al. 2005) but can also be influenced by the surface forcing dataset used to drive the LES. Second, the observed rCRE–f_C relationships are more variable. As demonstrated in section 4a(2), this is primarily due to a combination of the limited sampling density of the observations and 3D radiative effects. There is some suggestion of an opposite hysteresis in observations on all days other than 14 June 2017. It is difficult to determine whether this is a real feature or part of the variability in our limited sample of 4 days, but it should be investigated further as more cases become available in the future. Finally, we see a curious increase in observed rCRE at small f_C toward the end of all of the days. This could be another 3D radiative effect related to the larger fraction of radiation that will be intercepted by cloud sides and reflected back to space when the sun is lower in the sky, or simply because the atmosphere becomes more reflective when the sun is lower in the sky (Gristey et al. 2018). This effect was not seen in our 3D simulations of rCRE–f_C on the case-study day (Fig. 9d), but by this time of day the LES output had already returned to very small f_C.

5. Summary and conclusions

Utilizing LES and observations at the ARM SGP atmospheric observatory, shallow cumulus cloud fields

Downloaded from http://journals.ametsoc.org/jas/article-pdf/77/3/1065/4922254/jasd190261.pdf by NOAA Central Library user on 23 June 2020

and their surface shortwave radiative effects have been examined in detail. Focusing on a case-study day, 27 June 2015, and extending to multiple days, two meta-analyses of cloud fields and their radiative effects are investigated; PDFs of downwelling surface solar irradiance, and diurnal rCRE–f_C relationships. Both have proven to be useful and compact ways of condensing large amounts of data pertaining to radiatively relevant cloud properties. Moreover, their form can be directly connected to the underlying cloud processes.

Observed PDFs of downwelling surface solar irradiance under continental shallow cumuli are shown to exhibit bimodality. LES 1D radiation output does not reproduce this bimodality. However, bimodal PDFs emerge when the same LES cloud fields are ingested into offline 3D radiative transfer, demonstrating bimodality as a 3D radiative signature of continental shallow cumuli. This was found to result primarily from the diffuse radiation field. While scattered radiation by clouds in 1D is confined to the same model column in which the cloud shadow exists, radiation scattered in 3D reaches the surface in areas surrounding cloud shadows, resulting in a darkening of cloud shadows (i.e., first mode of the PDF) and a brightening between cloud shadows (i.e., second mode of the PDF). On the afternoon of the case-study day, local differences between 3D and 1D calculations of downwelling surface solar irradiance were found to be, on average, more than 150 $\mathrm{W\,m^{-2}}$. When averaged over the entire domain, differences were close to an order of magnitude smaller, but did not reach zero. Even when averaged over the diurnal cycle, the 3D bias in domain-mean downwelling surface solar irradiance was between 2 and 8 $\mathrm{W\,m^{-2}}$ on the days considered.

A well behaved and consistent diurnal relationship between rCRE and f_C is presented in domain-mean LES output. When f_C increases during the morning, rCRE is found to be smaller than when f_C decreases during the evening, resulting in a diurnal rCRE–f_C hysteresis that exists to various degrees on all simulated days. The same rCRE–f_C relationship derived from 1-min observations at the SGP Central Facility is highly variable. A 1-h running mean of the observations averaged over 10 nearby sites provides a more meaningful comparison with domain-mean LES quantities, but the diurnal hysteresis identified in LES is not present in observations on any of the days considered. Subsampling 3D radiative transfer calculations over the model grid revealed that an order of magnitude increase in the density of the observations would be needed to detect such relationships in reality. Overall, the rCRE–f_C framework for studying the evolution of shallow cumulus on a case-by-case basis is unlikely to be a practical for current observational networks, but exemplifies how high-resolution modeling can be used to reveal cloud field properties and processes not easily accessible from observations.

The importance of 3D radiative effects pervades our various analyses. The 3D biases in downwelling surface solar irradiance, and their variations with spatial and temporal scales, provide valuable insight for evaluating weather prediction and climate models against surface observations. Future work should consider how different cloud field properties influence the shape of the 3D downwelling surface solar irradiance distribution, and the subsequent biases relative to the equivalent 1D distribution. This will pave the way for model adjustments or additional parameterizations to account for 3D radiative effects, with possible implications for climate sensitivity. In addition, the magnitude of 3D biases presented here, together with previous work focusing on other cloud regimes, could have important implications for assessing solar renewable energy potential from model output in the future.

Acknowledgments. This work was supported by the National Oceanic and Atmospheric Administration (NOAA) Atmospheric Science for Renewable Energy (ASRE) program, and by the Office of Biological and Environmental Research of the U.S. Department of Energy Atmospheric System Research Program Interagency Agreement DE-SC0016275. Observations were obtained from the Atmospheric Radiation Measurement (ARM) Program, available at https://www.archive.arm.gov/discovery/. We thank Charles N. Long, who delivered a workshop on the Radiative Flux Analysis value-added product inspiring us to use those observations, and three anonymous reviewers for their valuable suggestions that helped to improve this manuscript.

REFERENCES

Angevine, W. M., J. Olson, J. Kenyon, W. I. Gustafson, S. Endo, K. Suselj, and D. D. Turner, 2018: Shallow cumulus in WRF parameterizations evaluated against LASSO large-eddy simulations. *Mon. Wea. Rev.*, **146**, 4303–4322, https://doi.org/10.1175/MWR-D-18-0115.1.

ARM, 2019a: Radiative Flux Analysis (RADFLUX1LONG). Southern Great Plains ARM Data Center, accessed 26 September 2019, https://doi.org/10.5439/1157585.

——, 2019b: Total Sky Imager (TSISKYIMAGE). Southern Great Plains Central Facility, accessed 4 September 2019, https://doi.org/10.5439/1025309.

Bender, F. A.-M., R. J. Charlson, A. M. L. Ekman, and L. V. Leahy, 2011: Quantification of monthly mean regional-scale albedo of marine stratiform clouds in satellite observations and GCMs. *J. Appl. Meteor. Climatol.*, **50**, 2139–2148, https://doi.org/10.1175/JAMC-D-11-049.1.

Downloaded from http://journals.ametsoc.org/jas/article-pdf/77/3/1065/4922254/jas190261.pdf by NOAA Central Library user on 23 June 2020

Benner, T. C., and K. F. Evans, 2001: Three-dimensional solar radiative transfer in small tropical cumulus fields derived from high-resolution imagery. *J. Geophys. Res.*, **106**, 14 975–14 984, https://doi.org/10.1029/2001JD900158.

Berg, L. K., and E. I. Kassianov, 2008: Temporal variability of fair-weather cumulus statistics at the ACRF SGP site. *J. Climate*, **21**, 3344–3358, https://doi.org/10.1175/2007JCLI2266.1.

——, ——, C. N. Long, and D. L. Mills, 2011: Surface summertime radiative forcing by shallow cumuli at the Atmospheric Radiation Measurement Southern Great Plains site. *J. Geophys. Res.*, **116**, D01202, https://doi.org/10.1029/2010JD014593.

Betts, A. K., and P. Viterbo, 2005: Land-surface, boundary layer, and cloud-field coupling over the southwestern Amazon in ERA-40. *J. Geophys. Res.*, **110**, D14108, https://doi.org/10.1029/2004JD005702.

Burleyson, C. D., C. N. Long, and J. M. Comstock, 2015: Quantifying diurnal cloud radiative effects by cloud type in the tropical western Pacific. *J. Appl. Meteor. Climatol.*, **54**, 1297–1312, https://doi.org/10.1175/JAMC-D-14-0288.1.

Clough, S. A., M. W. Shephard, E. J. Mlawer, J. S. Delamere, M. J. Iacono, K. Cady-Pereira, S. Boukabara, and P. D. Brown, 2005: Atmospheric radiative transfer modeling: A summary of the AER codes. *J. Quant. Spectrosc. Radiat. Transfer*, **91**, 233–244, https://doi.org/10.1016/j.jqsrt.2004.05.058.

Coddington, O., and Coauthors, 2008: Aircraft measurements of spectral surface albedo and its consistency with ground-based and space-borne observations. *J. Geophys. Res.*, **113**, D17209, https://doi.org/10.1029/2008JD010089.

Di Giuseppe, F., and A. M. Tompkins, 2003: Three-dimensional radiative transfer in tropical deep convective clouds. *J. Geophys. Res.*, **108**, 4741, https://doi.org/10.1029/2003JD003392.

Engström, A., F. A.-M. Bender, R. J. Charlson, and R. Wood, 2015: The nonlinear relationship between albedo and cloud fraction on near-global, monthly mean scale in observations and in the CMIP5 model ensemble. *Geophys. Res. Lett.*, **42**, 9571–9578, https://doi.org/10.1002/2015GL066275.

Feingold, G., A. McComiskey, T. Yamaguchi, J. S. Johnson, K. S. Carslaw, and K. S. Schmidt, 2016: New approaches to quantifying aerosol influence on the cloud radiative effect. *Proc. Natl. Acad. Sci. USA*, **113**, 5812–5819, https://doi.org/10.1073/pnas.1514035112.

——, J. Balsells, F. Glassmeier, T. Yamaguchi, J. Kazil, and A. McComiskey, 2017: Analysis of albedo versus cloud fraction relationships in liquid water clouds using heuristic models and large eddy simulation. *J. Geophys. Res. Atmos.*, **122**, 7086–7102, https://doi.org/10.1002/2017JD026467.

Fielding, M. D., J. C. Chiu, R. J. Hogan, and G. Feingold, 2014: A novel ensemble method for retrieving properties of warm cloud in 3-D using ground-based scanning radar and zenith radiances. *J. Geophys. Res. Atmos.*, **119**, 10 912–10 930, https://doi.org/10.1002/2014JD021742.

Forster, L., C. Emde, B. Mayer, and S. Unterstrasser, 2012: Effects of three-dimensional photon transport on the radiative forcing of realistic contrails. *J. Atmos. Sci.*, **69**, 2243–2255, https://doi.org/10.1175/JAS-D-11-0206.1.

Glenn, I. B., G. Feingold, J. J. Gristey, and T. Yamaguchi, 2019: Quantification of the radiative effect of aerosol–cloud interactions in shallow continental cumulus clouds. *J. Atmos. Sci.*, submitted.

Gounou, A., and R. J. Hogan, 2007: A sensitivity study of the effect of horizontal photon transport on the radiative forcing of contrails. *J. Atmos. Sci.*, **64**, 1706–1716, https://doi.org/10.1175/JAS3915.1.

Gristey, J. J., J. C. Chiu, R. J. Gurney, C. J. Morcrette, P. G. Hill, J. E. Russell, and H. E. Brindley, 2018: Insights into the diurnal cycle of global Earth outgoing radiation using a numerical weather prediction model. *Atmos. Chem. Phys.*, **18**, 5129–5145, https://doi.org/10.5194/acp-18-5129-2018.

Gronemeier, T., F. Kanani-Sühring, and S. Raasch, 2017: Do shallow cumulus clouds have the potential to trigger secondary circulations via shading? *Bound.-Layer Meteor.*, **162**, 143–169, https://doi.org/10.1007/s10546-016-0180-7.

Gustafson, W. I., and Coauthors, 2019: Description of the LASSO data bundles product. OSTI.GOV Tech. Rep. DOE/SC-ARM-TR-216, 122 pp., https://doi.org/10.2172/1469590.

——, and Coauthors, 2020: The Large-Eddy Simulation (LES) Atmospheric Radiation Measurement (ARM) Symbiotic Simulation and Observation (LASSO) workflow for continental shallow convection. *Bull. Amer. Meteor. Soc.*, https://doi.org/10.1175/BAMS-D-19-0065.1, in press.

Ham, S.-H., S. Kato, H. W. Barker, F. G. Rose, and S. Sun-Mack, 2014: Effects of 3-D clouds on atmospheric transmission of solar radiation: Cloud type dependencies inferred from A-train satellite data. *J. Geophys. Res. Atmos.*, **119**, 943–963, https://doi.org/10.1002/2013JD020683.

Hinkelman, L. M., K. F. Evans, E. E. Clothiaux, T. P. Ackerman, and P. W. Stackhouse, 2007: The effect of cumulus cloud field anisotropy on domain-averaged solar fluxes and atmospheric heating rates. *J. Atmos. Sci.*, **64**, 3499–3520, https://doi.org/10.1175/JAS4032.1.

Hogan, R. J., and J. K. P. Shonk, 2013: Incorporating the effects of 3D radiative transfer in the presence of clouds into two-stream multilayer radiation schemes. *J. Atmos. Sci.*, **70**, 708–724, https://doi.org/10.1175/JAS-D-12-041.1.

——, M. D. Fielding, H. W. Barker, N. Villefranque, and S. A. K. Schäfer, 2019: Entrapment: An important mechanism to explain the shortwave 3D radiative effect of clouds. *J. Atmos. Sci.*, **76**, 2123–2141, https://doi.org/10.1175/JAS-D-18-0366.1.

Iwabuchi, H., 2006: Efficient Monte Carlo methods for radiative transfer modeling. *J. Atmos. Sci.*, **63**, 2324–2339, https://doi.org/10.1175/JAS3755.1.

Jakub, F., and B. Mayer, 2017: The role of 1-D and 3-D radiative heating in the organization of shallow cumulus convection and the formation of cloud streets. *Atmos. Chem. Phys.*, **17**, 13 317–13 327, https://doi.org/10.5194/acp-17-13317-2017.

Kassianov, E., C. N. Long, and M. Ovtchinnikov, 2005: Cloud sky cover versus cloud fraction: Whole-sky simulations and observations. *J. Appl. Meteor.*, **44**, 86–98, https://doi.org/10.1175/JAM-2184.1.

Khairoutdinov, M. F., and D. A. Randall, 2003: Cloud resolving modeling of the ARM summer 1997 IOP: Model formulation, results, uncertainties, and sensitivities. *J. Atmos. Sci.*, **60**, 607–625, https://doi.org/10.1175/1520-0469(2003)060<0607:CRMOTA>2.0.CO;2.

Lamer, K., and P. Kollias, 2015: Observations of fair-weather cumuli over land: Dynamical factors controlling cloud size and cover. *Geophys. Res. Lett.*, **42**, 8693–8701, https://doi.org/10.1002/2015GL064534.

Lane, D. E., K. Goris, and R. C. J. Somerville, 2002: Radiative transfer through broken clouds: Observations and model validation. *J. Climate*, **15**, 2921–2933, https://doi.org/10.1175/1520-0442(2002)015<2921:RTTBCO>2.0.CO;2.

Liu, Y., W. Wu, M. P. Jensen, and T. Toto, 2011: Relationship between cloud radiative forcing, cloud fraction and cloud albedo, and new surface-based approach for determining cloud

Downloaded from http://journals.ametsoc.org/jas/article-pdf/77/3/1065/4922254/jas190261.pdf by NOAA Central Library user on 23 June 2020

albedo. *Atmos. Chem. Phys.*, **11**, 7155–7170, https://doi.org/10.5194/acp-11-7155-2011.

Long, C. N., and T. P. Ackerman, 2000: Identification of clear skies from broadband pyranometer measurements and calculation of downwelling shortwave cloud effects. *J. Geophys. Res.*, **105**, 15 609–15 626, https://doi.org/10.1029/2000JD900077.

——, ——, K. L. Gaustad, and J. N. S. Cole, 2006: Estimation of fractional sky cover from broadband shortwave radiometer measurements. *J. Geophys. Res.*, **111**, D11204, https://doi.org/10.1029/2005JD006475.

McClatchey, R. A., R. W. Fenn, J. E. A. Selby, F. E. Volz, and J. S. Garin, 1972: *Optical Properties of the Atmosphere*. 3rd ed. Air Force Cambridge Research Labs, 108 pp.

Mlawer, E. J., S. J. Taubman, P. D. Brown, M. J. Iacono, and S. A. Clough, 1997: Radiative transfer for inhomogeneous atmospheres: RRTM, a validated correlated-*k* model for the longwave. *J. Geophys. Res.*, **102**, 16 663–16 682, https://doi.org/10.1029/97JD00237.

O'Hirok, W., and C. Gautier, 2005: The impact of model resolution on differences between independent column approximation and Monte Carlo estimates of shortwave surface irradiance and atmospheric heating rate. *J. Atmos. Sci.*, **62**, 2939–2951, https://doi.org/10.1175/JAS3519.1.

Oue, M., P. Kollias, K. W. North, A. Tatarevic, S. Endo, A. M. Vogelmann, and W. I. Gustafson, 2016: Estimation of cloud fraction profile in shallow convection using a scanning cloud radar. *Geophys. Res. Lett.*, **43**, 10 998–11 006, https://doi.org/10.1002/2016GL070776.

Perez, R., M. David, T. E. Hoff, M. Jamaly, S. Kivalov, J. Kleissl, P. Lauret, and M. Perez, 2016: Spatial and temporal variability of solar energy. *Found. Trends Renewable Energy*, **1**, 1–44, https://doi.org/10.1561/2700000006.

Pincus, R., C. Hannay, and K. F. Evans, 2005: The accuracy of determining three-dimensional radiative transfer effects in cumulus clouds using ground-based profiling instruments. *J. Atmos. Sci.*, **62**, 2284–2293, https://doi.org/10.1175/JAS3464.1.

Schmidt, K. S., G. Feingold, P. Pilewskie, H. Jiang, O. Coddington, and M. Wendisch, 2009: Irradiance in polluted cumulus fields: Measured and modeled cloud-aerosol effects. *Geophys. Res. Lett.*, **36**, L07804, https://doi.org/10.1029/2008GL036848.

Sena, E. T., A. Mccomiskey, and G. Feingold, 2016: A long-term study of aerosol-cloud interactions and their radiative effect at the Southern Great Plains using ground-based measurements. *Atmos. Chem. Phys.*, **16**, 11 301–11 318, https://doi.org/10.5194/acp-16-11301-2016.

Song, S., and Coauthors, 2016: The spectral signature of cloud spatial structure in shortwave irradiance. *Atmos. Chem. Phys.*, **16**, 13 791–13 806, https://doi.org/10.5194/acp-16-13791-2016.

Stephens, G. L., and Coauthors, 2012: An update on Earth's energy balance in light of the latest global observations. *Nat. Geosci.*, **5**, 691–696, https://doi.org/10.1038/ngeo1580.

Stoffel, T., 2005: Solar Infrared Radiation Station (SIRS) Handbook. Atmospheric Radiation Measurement Climate Research Facility Rep. ARM TR-025, 32 pp.

Trenberth, K. E., and J. T. Fasullo, 2012: Tracking Earth's energy: From El Niño to global warming. *Surv. Geophys.*, **33**, 413–426, https://doi.org/10.1007/s10712-011-9150-2.

Várnai, T., 2000: Influence of three-dimensional radiative effects on the spatial distribution of shortwave cloud reflection. *J. Atmos. Sci.*, **57**, 216–229, https://doi.org/10.1175/1520-0469(2000)057<0216:IOTDRE>2.0.CO;2.

——, and R. Davies, 1999: Effects of cloud heterogeneities on shortwave radiation: Comparison of cloud-top variability and internal heterogeneity. *J. Atmos. Sci.*, **56**, 4206–4224, https://doi.org/10.1175/1520-0469(1999)056<4206:EOCHOS>2.0.CO;2.

Wild, M., and Coauthors, 2015: The energy balance over land and oceans: An assessment based on direct observations and CMIP5 climate models. *Climate Dyn.*, **44**, 3393–3429, https://doi.org/10.1007/s00382-014-2430-z.

Xiao, H., L. K. Berg, and M. Huang, 2018: The impact of surface heterogeneities and land-atmosphere interactions on shallow clouds over ARM SGP site. *J. Adv. Model. Earth Syst.*, **10**, 1220–1244, https://doi.org/10.1029/2018MS001286.

Xie, S., R. T. Cederwall, and M. Zhang, 2004: Developing long-term single-column model/cloud system–resolving model forcing data using numerical weather prediction products constrained by surface and top of the atmosphere observations. *J. Geophys. Res.*, **109**, D01104, https://doi.org/10.1029/2003JD004045.

Xie, Y., Y. Liu, C. N. Long, and Q. Min, 2014: Retrievals of cloud fraction and cloud albedo from surface-based shortwave radiation measurements: A comparison of 16 year measurements. *J. Geophys. Res. Atmos.*, **119**, 8925–8940, https://doi.org/10.1002/2014JD021705.

Zhang, Y., S. A. Klein, J. Fan, A. S. Chandra, P. Kollias, S. Xie, and S. Tang, 2017: Large-eddy simulation of shallow cumulus over land: A composite case based on ARM long-term observations at its Southern Great Plains site. *J. Atmos. Sci.*, **74**, 3229–3251, https://doi.org/10.1175/JAS-D-16-0317.1.

Zhong, W., R. J. Hogan, and J. D. Haigh, 2008: Three-dimensional radiative transfer in midlatitude cirrus clouds. *Quart. J. Roy. Meteor. Soc.*, **134**, 199–215, https://doi.org/10.1002/qj.182.

Downloaded from http://journals.ametsoc.org/jas/article-pdf/77/3/1065/4922254/jas190261.pdf by NOAA Central Library user on 23 June 2020